Slip Systems in MgSiO3 Post-Perovskite: Implications for D'' Anisotropy

Lowell Miyagi, *et al.*

Science **329**, 1639 (2010);
DOI: 10.1126/science.1192465

This copy is for your personal, non-commercial use only.

If you wish to distribute this article to others, you can order high-quality copies for your colleagues, clients, or customers by clicking here.

Permission to republish or repurpose articles or portions of articles can be obtained by following the guidelines here.

The following resources related to this article are available online at www.sciencemag.org (this information is current as of September 28, 2010):

Updated information and services, including high-resolution figures, can be found in the online version of this article at:
http://www.sciencemag.org/cgi/content/full/329/5999/1639

Supporting Online Material can be found at:
http://www.sciencemag.org/cgi/content/full/329/5999/1639/DC1

This article **cites 35 articles**, 8 of which can be accessed for free:
http://www.sciencemag.org/cgi/content/full/329/5999/1639#otherarticles

This article appears in the following **subject collections**:
Geochemistry, Geophysics
http://www.sciencemag.org/cgi/collection/geochem_phys

Science (print ISSN 0036-8075; online ISSN 1095-9203) is published weekly, except the last week in December, by the American Association for the Advancement of Science, 1200 New York Avenue NW, Washington, DC 20005. Copyright 2010 by the American Association for the Advancement of Science; all rights reserved. The title *Science* is a registered trademark of AAAS.

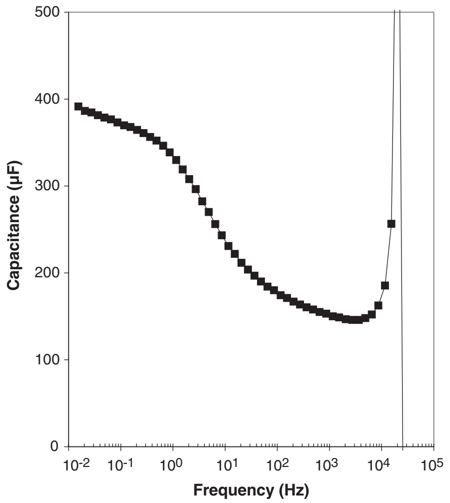

Fig. 4. Capacitance versus frequency of the graphene nanosheet DLC, assuming a series-RC circuit model. Capacitive behavior is shown up to ~10^4 Hz.

inary part of the impedance. Capacitance versus frequency from this equation is plotted in Fig. 4 for the graphene nanosheet capacitor shown in the previous figures. At 120 Hz, the derived capacitance value is 175 μF, and the measured resistance is 1.1 ohms, yielding an RC time constant of less than 200 μs. Divergent behavior near 20 kHz is an artifact of the model (where Z'' passes through zero) and should be ignored. As shown, the capacitance value increases from ~175 μF in the 10- to 10^4-Hz band up to ~375 μF at frequencies below ~1 Hz. The increase occurs in the region of the phase angle dip shown in Fig. 3. Capacitance saturation (horizontal behavior) was not observed even at 0.01 Hz, although this device exhibited incredibly fast response, suggesting the involvement of a second, much-lower-rate charge-storage process. Three-electrode measurements revealed that the positive electrode had greater capacitance increase at low frequency than did the negative electrode. Capacitors of the same design fabricated by using bare Ni electrodes had capacitance values of less than 25 μF at 120 Hz. We attribute the marked capacitance increase at low frequency to pseudocapacitance derived from ion intercalation into the exposed edge planes of the graphene structure. Pseudocapacitance by this mechanism has been reported for exfoliated carbon fibers with sulfuric acid electrolyte (*20*).

A similar vertically oriented graphene nanosheet capacitor fabricated with an organic electrolyte (1 M tetraethylammonium-tetrafluoroborate salt in propylene carbonate) showed more definite but still incomplete saturation of capacitance at low frequency (fig. S1). The organic electrolyte capacitance was ~50% higher than the value from aqueous electrolyte prototypes, which is opposite to typical activated carbon behavior. This boost in capacitance using the organic electrolyte may result from more complete wetting of the graphene nanosheet surface with this electrolyte.

Capacitance at 120 Hz was ~175 μF for the graphene nanosheet capacitor (with KOH electrolyte), which corresponds to a capacitance density of the 0.6-μm-thick active layer of ~3 F/cm^3. The graphene active layer stored ~1.5 FV/cm^3 with the aqueous electrolyte (0.5 V) and ~5.5 FV/cm^3 with the organic electrolyte (1.25 V). Aluminum electrolytic capacitor foil is highly etched before being anodized so as to create charge storage throughout its volume. Low-voltage aluminum anode foil (KDK, Tokyo, Japan) has CV/volume values up to ~0.14 FV/cm^3. Thus, a graphene DLC in principal could have substantially smaller volume than a comparably rated low-voltage aluminum electrolytic capacitor.

DLC designs would differ from the spiral-wound construction commonly used with aluminum electrolytic capacitors because of operating voltage differences. A bipolar design (cell stacking), as presently used by several DLC manufacturers, offers volumetric efficiency and may be optimal. With stacked cells, DLC capacitance density scales like the inverse of the square of the number of series-connected cells: ~$1/V^2$, where V is the device operating voltage. Capacitance density of an electrolytic capacitor scales like 1/V because the CV product of anodic dielectric is approximately constant. Thus, DLC capacitance density advantages will disappear at a particular voltage. Using prototype performance measurements with conventional construction materials in a practical design (fig. S2), a single-cell graphene DLC (~2.5 V operation) should offer a sixfold or greater volume advantage over an aluminum electrolytic capacitor of the same rating. A two-cell graphene DLC (~5 V operation) should offer a twofold or greater volume advantage over an equivalently rated aluminum electrolytic capacitor. No volumetric advantages are expected at higher voltage. Aluminum electrolytic capacitors rated at 2 V or higher are widely used today for bypass and filtering in portable electronics equipment.

Graphene nanosheet electrodes could be manufactured by using standard semiconductor process equipment. The fabrication of the electrode and the choice of electrolyte have not been optimized, and increases in capacitance density through further optimization appear likely. Cell operating voltage may be increased with ionic liquid electrolytes or by use of an asymmetric design, with either approach expanding the voltage region in which the graphene DLC capacitance density exceeds that of present aluminum electrolytic capacitor technology.

References and Notes

1. B. E. Conway, *Electrochemical Supercapacitors: Scientific Fundamentals and Technological Applications* (Kluwer Academic/Plenum, New York, 1999).
2. J. R. Miller, A. F. Burke, *Electrochem. Soc. Interface* **17**, 53 (2008).
3. J. R. Miller, *Batt. Ener. Stor. Technol.* **18**, 61 (2007).
4. A. F. Burke, J. E. Hardin, E. J. Dowgiallo, "Applications of Ultracapacitors in Electric Vehicle Propulsion Systems," presented at the 34th Power Sources Conference, Cherry Hill, NJ (1990).
5. J. R. Miller, P. Simon, *Science* **321**, 651 (2008).
6. D. L. Boos, S. D. Argade, "Historical Background and New Perspectives for Double-Layer Capacitors," presented at the 1st International Seminar on Double Layer Capacitors and Similar Energy Storage Devices, Deerfield Beach, FL (1991).
7. R. de Levie, P. Delahay, C. W. Tobias, Eds., *Advances in Electrochemistry and Electrochemical Engineering* (Interscience, New York, 1967).
8. C. Niu, E. K. Sichel, R. Hoch, D. Moy, H. Tennent, *Appl. Phys. Lett.* **70**, 1480 (1997).
9. C. Du, N. Pan, *J. Power Sources* **160**, 1487 (2006).
10. C. Du, N. Pan, *Nanotechnology* **17**, 5314 (2006).
11. C. Du, N. Pan, *Nanotechnol. Law Bus.* **4**, 569 (2007).
12. J. Schindall, J. Kassakian, R. Signorelli, paper presented at the 2007 Advanced Capacitor World Summit, San Diego, CA (2007).
13. Y. Honda *et al.*, *Electrochem. Solid-State Lett.* **10**, A106 (2007).
14. M. D. Stoller, S. Park, Y. Zhu, J. An, R. S. Ruoff, *Nano Lett.* **8**, 3498 (2008).
15. X. Zhao *et al.*, *J. Power Sources* **194**, 1208 (2009).
16. J. P. Randin, E. Yeager, *J. Electrochem. Soc.* **118**, 711 (1971).
17. J. Wang *et al.*, *Appl. Phys. Lett.* **85**, 1265 (2004).
18. M. Zhu *et al.*, *Carbon* **45**, 2229 (2007).
19. I. D. Raistrick, in *Electrochemistry of Semiconductors and Electronics*, J. McHardy, F. Ludwig, Eds. (Noyes Publications, Park Ridge, NJ, 1992), pp. 297–355.
20. Y. Sonedaa *et al.*, *J. Phys. Chem. Solids* **65**, 219 (2004).
21. This work was supported in part by DARPA Defense Sciences Office, 3701 N. Fairfax Dr., Arlington, VA 22203.

Supporting Online Material
www.sciencemag.org/cgi/content/full/329/5999/1637/DC1
Figs. S1 and S2

28 June 2010; accepted 19 August 2010
10.1126/science.1194372

Slip Systems in $MgSiO_3$ Post-Perovskite: Implications for *D*″ Anisotropy

Lowell Miyagi,[1] Waruntorn Kanitpanyacharoen,[2] Pamela Kaercher,[2]
Kanani K. M. Lee,[1] Hans-Rudolf Wenk[2]*

Understanding deformation of mineral phases in the lowermost mantle is important for interpreting seismic anisotropy in Earth's interior. Recently, there has been considerable controversy regarding deformation-induced slip in $MgSiO_3$ post-perovskite. Here, we observe that (001) lattice planes are oriented at high angles to the compression direction immediately after transformation and before deformation. Upon compression from 148 gigapascals (GPa) to 185 GPa, this preferred orientation more than doubles in strength, implying slip on (001) lattice planes. This contrasts with a previous experiment that recorded preferred orientation likely generated during the phase transformation rather than deformation. If we use our results to model deformation and anisotropy development in the *D*″ region of the lower mantle, shear-wave splitting (characterized by fast horizontally polarized shear waves) is consistent with seismic observations.

The *D*″ region lies just above the core mantle boundary (CMB). In contrast to the bulk of the lower mantle, this ~200-km-thick layer possesses apparent seismic complexity, including seismic discontinuity, large topographic variations, lateral heterogeneity, variable anisotropy, and ultralow velocity zones (*1*–*4*). The *D*″ region is of great interest from a geodynamic perspective because it is a boundary layer between two regions with extreme viscosity contrasts (i.e., the solid mantle and liquid outer core). As such, it should play an active role in controlling mantle convection, thermal structure, and evolution of Earth (*5*). Numerical modeling (*6*) and laboratory experiments (*7*) indicate that deformation is enhanced near boundary layers, and large strain deformation is expected to occur in the *D*″ region, particularly in slabs subducted to the CMB. Thus, it is likely that seismic anisotropies observed in this region are produced by deformation-induced texturing (preferred orientation) of the constituent minerals (*2*, *6*, *7*).

The discovery of a solid-solid phase transition in $MgSiO_3$ from a perovskite (Pv) to a post-perovskite (pPv) structure at conditions closely corresponding to those of the CMB (127 GPa and 2500 K) provided a new perspective for interpreting the *D*″ layer (*8*–*10*). However, several issues remain unresolved, including how texture develops in pPv and how the deformation state in the *D*″ is expressed as seismic anisotropy. Texture may be important in explaining the sharpness of the *D*″ discontinuity (*11*); seismological observations suggest the thickness of the discontinuity to be less than 30 km (*12*), but experimental data predicts that the thicknesses should be on the order of 90 km for an isotropic aggregate (*13*–*15*).

When stress is applied to a polycrystal, individual crystals deform preferentially along slip planes. This results in crystal rotations that in turn lead to preferred orientation of the polycrystal (texture). Because individual crystals are anisotropic, texturing can result in bulk anisotropy. Previous deformation experiments on $MgSiO_3$ pPv and the $MgGeO_3$ pPv analog produced textures consistent with slip on {110} and/or (100) planes (*16*, *17*); however, these slip systems are expected to generate anisotropy largely incompatible with seismic observations. The older experiments showed that texture developed during conversion to the pPv phase and that further compression did not result in textural changes (*16*, *17*). Recently, Okada *et al.* (*18*) performed new experiments on $MgGeO_3$ pPv. After transformation from the Pv to pPv phase, (001) planes were oriented at high angles to compression. When $MgGeO_3$ enstatite was used as a starting material, axial diffraction patterns consistent with the textures of Merkel *et al.* (*16*, *17*) were observed. After further compression, it appeared that (001) planes became aligned normal to compression, implying that the former texture is related to the phase transformation (*18*).

In the $CaIrO_3$ pPv analog, however, the dominant slip plane is (010) over a range of pressures, temperatures, and strain rates (*19*, *20*–*23*). This differing slip system may arise due to bonding differences in $CaIrO_3$ pPv from other pPv structured compounds (*24*). First-principles computations also find $CaIrO_3$ pPv to have elastic properties and an electronic structure that are different from $MgSiO_3$ pPv (*25*), and modeling of dislocation cores predicts that $CaIrO_3$ is much more plastically anisotropic than $MgSiO_3$ pPv (*26*, *27*).

We performed axial compression experiments on $MgSiO_3$ pPv between 148 GPa and 185 GPa in the diamond anvil cell (DAC). The evolution of texture and lattice strains were recorded in situ, using monochromatic synchrotron x-ray diffraction in radial geometry. The starting material of vitreous $MgSiO_3$ was mixed with ~10 weight percent Pt powder to serve as a laser absorber and a pressure standard, and was compressed to high pressure (*28*). Conversion directly to the pPv phase was obtained by laser heating at ~3500 K for ~10 min (*28*). After conversion to pPv, pressure in the sample was 148 GPa (table S2). Pressure was then increased in four steps to 185 GPa over the course of 7 hours (table S2). At each step, in situ radial x-ray diffraction images were collected to document the evolution of pressure, differential stress, and texture.

Radial diffraction images show variations in peak position with respect to the compression direction, which indicate elastic stresses imposed by the DAC, as well as systematic intensity variations, which denote texture. These variations are best visualized if the image is unrolled to display azimuth versus diffraction angle (Fig. 1). To quantitatively extract texture information and calculate differential stress, we use the Rietveld method as implemented in the software package MAUD (*28*, *29*). After conversion, at 148 GPa, differential stress was 5.3 ± 0.1 GPa. At the highest pressure attained, 185 GPa, the differential stress was 10.9 ± 0.5 GPa (table S2). Inverse pole figures (IPF) of the compression direction show the probability of finding the pole (normal) to a lattice plane in the compression direction (Fig. 2). Just after conversion to pPv, the sample exhibits a texture characterized by (001) lattice planes at high angles to compression, with an IPF maximum of 4.09 multiples of a random distribution (m.r.d.) (Fig. 2A and table S2). After the first compression step to 164 GPa, the strength of the 001 maximum increases dramatically to 9.62 m.r.d. (Fig. 2B and table S2). Between 164 GPa and 185 GPa, texture changes very little (Fig. 2, B and C, and table S2). This differs from textures recorded in lower-pressure pPv analogs of Mn_2O_3 (*30*), $CaIrO_3$ (*19*, *20*–*23*), $MgGeO_3$ (*16*), and $MgSiO_3$ (*17*) but is consistent with the most recent measurements on $MgGeO_3$ pPv (*18*). These textures are stronger than textures recorded in previous experiments (*16*, *17*). In this experiment, texture strength after compression is greater than 9 m.r.d. versus ~2.5 m.r.d. in $MgSiO_3$ pPv (*17*), ~2.5 m.r.d. in $MgGeO_3$ pPv (*30*), and ~1.8 m.r.d. in $CaIrO_3$ pPv (*23*). The present results cannot be directly compared with the results of Okada *et al.* (*18*) because those measurements were qualitative.

In contrast to a previous DAC experiment on $MgSiO_3$ pPv (*17*), we observe a texture evolution with compression and conclude that the strengthening of the 001 texture is due to plastic

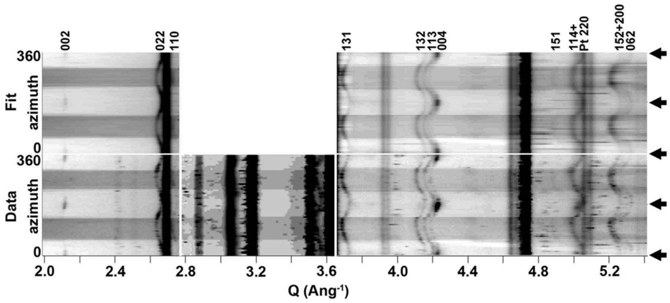

Fig. 1. "Unrolled" diffraction image of $MgSiO_3$ pPv taken in situ at 185 GPa (bottom) with the fit from Rietveld refinement (top). The region from 2.77 to 3.66 Å^{-1} was excluded from Rietveld refinement due to very intense diffraction from the gasket and little signal from the sample. pPv diffraction peaks are labeled, and black arrows indicate the compression direction. Straight lines are from the gasket. The Pt 220 peak is also labeled and overlaps with the sample. Pt 111 and 200 are buried in the gasket peaks. There may also be some minor formation of PtC due to the reaction of Pt with the diamonds during laser heating (*28*). Texture is evident as systematic intensity variations along diffraction peaks. For example, pPv 004 has a strong maximum in the compression direction. Deviatoric stress can be calculated from the variation of peak position with azimuth, which is observed in the diffraction image.

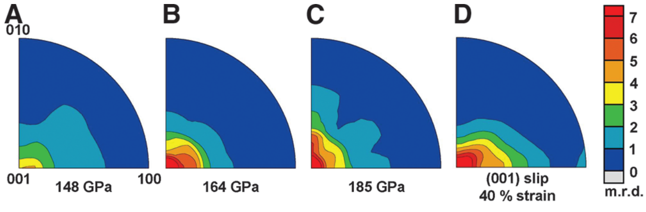

Fig. 2. Inverse pole figures of $MgSiO_3$ pPv at 148 GPa (**A**) just after transformation and at two pressure steps up to 185 GPa (**C**). Also shown for comparison is an IPF of VPSC results for dominant slip on (001) and 40% compressive strain (**D**). This provides a good match to the data after compression (**B** and **C**). Equal area projection and a linear scale is used. Scale bar in m.r.d., where m.r.d. = 1 is random and a higher m.r.d. number indicates stronger texture.

---

[1]Department of Geology and Geophysics, Yale University, New Haven, CT 06511, USA. [2]Department of Earth and Planetary Science, University of California, Berkeley, CA 94720, USA.

*To whom correspondence should be addressed. E-mail: wenk@berkeley.edu

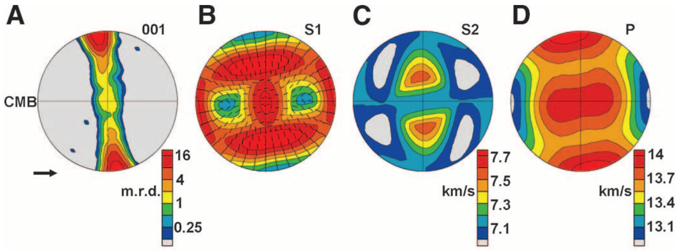

Fig. 3. Equal area projection pole figures showing texture development and anisotropic elastic properties of a pPv aggregate in a subducting slab near the core-mantle boundary using deformation mechanisms established in this study. (**A**) (001) pole figure of pPv showing a snapshot during spreading in a plane strain regime (i.e., intermediate between pure shear and simple shear). (**B**) Fast shear-wave velocities and polarization. (**C**) Slow shear-wave velocities. (**D**) *P* wave velocity surface. Flow direction indicated by arrow.

deformation. Deformation of pPv has been extensively modeled using the viscoplastic self-consistent polycrystal plasticity code [VPSC; (*31*)] (*16*, *17*, *23*). A comparison of the IPFs obtained in this study with results of VPSC models shows that the 001 texture observed here is compatible with dominant slip on (001) lattice planes and 40% compressive strain (Fig. 2D). For this model, the transformation texture obtained after conversion to pPv was used as the starting texture for the deformation simulation (Fig. 2A).

Admittedly, there are limitations to our experiments because the time scale of deformation, grain size, composition, temperature, and deviatoric stress are quite different from those expected in the *D*″. However, if we assume that slip is active on (001) planes in MgSiO$_3$ pPv at *D*″ conditions and combine this information with geodynamic modeling of deformation along the *D*″, we can predict texture development in the lowermost mantle. This can, in turn, be combined with single crystal elastic constants to assess associated seismic anisotropy. For these calculations, we neglect any contribution from the second most abundant mineral in the mantle, ferropericlase, which may also play an important role in generating *D*″ anisotropy (*32*).

In this context, we use information from the same two-dimensional geodynamic model applied previously (*17*, *33*) to predict texture development in a slab subducted into the *D*″ zone. A tracer records the strain-temperature history and, accordingly, the texture evolution is modeled with the same polycrystal plasticity theory applied to the experiment (*31*). It is assumed that the aggregate has a random orientation distribution as it enters the *D*″ about 290 km above the CMB. Based on our results, we assume dominant (001)[100] and (001)[010] slip. We chose a geodynamic tracer that records strain and temperature, which advances close to the CMB and attains large strains. Preferred orientation develops rapidly and then stabilizes; note the strong alignment of (001) lattice planes slightly inclined to the CMB (Fig. 3A). By averaging the orientation distribution and single crystal elastic properties (*34*), we calculated aggregate elastic properties and seismic wave propagation. Based on the polarization directions of the fast and slow shear-wave velocities, high shear-wave splitting is 0.55 km/s in the flow direction; fast shear waves are polarized parallel to the CMB (Fig. 3B, C). This is consistent with seismic observations of the circum-Pacific regions (*2*, *4*), where the presence of pPv is expected (*35*, *36*). The anticorrelation between fast *S* waves and *P* waves in the flow direction (Fig. 3D) is also consistent with seismic records (*37*, *38*).

References and Notes

1. D. Helmberger, T. Lay, S. Ni, M. Gurnis, *Proc. Natl. Acad. Sci. U.S.A.* **102**, 17257 (2005).
2. J. Wookey, J. Kendall, in *Post-Perovskite: The Last Mantle Phase Transition*, K. Hirose, D. Yuen, T. Lay, J. P. Brodholt, Eds. (American Geophysical Union, Washington DC, 2007), pp. 171–189.
3. E. J. Garnero, A. K. McNamara, *Science* **320**, 626 (2008).
4. M. Panning, B. Romanowicz, *Science* **303**, 351 (2004).
5. P. J. Tackley, *Science* **288**, 2002 (2000).
6. A. K. McNamara, P. E. V. Keken, S. Karato, *J. Geophys. Res.* **108**, (B5), 2230 (2003).
7. N. Loubet, N. M. Ribe, Y. Gamblin, *Geochem. Geophys. Geosyst.* **10**, Q10004 (2009).
8. M. Murakami, K. Hirose, K. Kawamura, N. Sata, Y. Ohishi, *Science* **304**, 855 (2004).
9. A. R. Oganov, S. Ono, *Nature* **430**, 445 (2004).
10. S. Shim, T. S. Duffy, R. Jeanloz, G. Shen, *Geophys. Res. Lett.* **31**, L10603 (2004).
11. M. Murakami, K. Hirose, N. Sata, Y. Ohishi, *Geophys. Res. Lett.* **32**, L03304 (2005).
12. T. Lay, *Geophys. Res. Lett.* **35**, L03304 (2008).
13. K. Ohta, K. Hirose, N. Sata, Y. Ohishi, *Geochim. Cosmochim. Acta* **70**, A454 (2006).
14. K. Catalli, S. H. Shim, V. Prakapenka, *Nature* **462**, 782 (2009).
15. D. Andrault *et al.*, *Earth Planet. Sci. Lett.* **293**, 90 (2010).
16. S. Merkel *et al.*, *Science* **311**, 644 (2006).
17. S. Merkel *et al.*, *Science* **316**, 1729 (2007).
18. T. Okada, T. Yagi, K. Niwa, T. Kikegawa, *Phys. Earth Planet. Inter.* **180**, 195 (2010).
19. N. P. Walte *et al.*, *Geophys. Res. Lett.* **36**, L04302 (2009).
20. N. Miyajima, K. Ohgushi, M. Ichihara, T. Yagi, *Geophys. Res. Lett.* **33**, L12302 (2006).
21. D. Yamazaki, T. Yoshino, H. Ohfuji, J. Ando, A. Yoneda, *Earth Planet. Sci. Lett.* **252**, 372 (2006).
22. K. Niwa *et al.*, *Phys. Chem. Miner.* **34**, 679 (2007).
23. L. Miyagi *et al.*, *Earth Planet. Sci. Lett.* **268**, 515 (2008).
24. J. Hustoft, S. Shim, A. Kubo, N. Nishiyama, *Am. Mineral.* **93**, 1654 (2008).
25. T. Tsuchiya, J. Tsuchiya, *Phys. Rev. B* **76**, 144119 (2007).
26. P. Carrez, D. Ferré, P. Cordier, *Philos. Mag.* **87**, 3229 (2007).
27. A. Metsue, P. Carrez, D. Mainprice, P. Cordier, *Phys. Earth Planet. Inter.* **174**, 165 (2009).
28. Materials and methods are available as supporting material on *Science* Online.
29. L. Lutterotti, S. Matthies, H. Wenk, A. S. Schultz, J. W. Richardson, *J. Appl. Phys.* **81**, 594 (1997).
30. J. Santillán, S. Shim, G. Shen, V. B. Prakapenka, *Geophys. Res. Lett.* **33**, L15307 (2006).
31. R. Lebensohn, C. Tomé, *Mater. Sci. Eng. A* **175**, 71 (1994).
32. M. D. Long, X. Xiao, Z. Jiang, B. Evans, S. Karato, *Phys. Earth Planet. Inter.* **156**, 75 (2006).
33. A. K. McNamara, S. Zhong, *Nature* **437**, 1136 (2005).
34. S. Stackhouse, J. P. Brodholt, J. Wookey, J. Kendall, G. D. Price, *Earth Planet. Sci. Lett.* **230**, 1 (2005).
35. J. W. Hernlund, C. Thomas, P. J. Tackley, *Nature* **434**, 882 (2005).
36. R. D. van der Hilst *et al.*, *Science* **315**, 1813 (2007).
37. G. Masters, G. Laske, H. Bolton, A. M. Dziewonski, in *Earth's Deep Interior: Mineral Physics and Tomography From the Atomic to Global Scale*, S.-I. Karato, A. M. Forte, R. C. Liebermann, G. Masters, L. Stixrude, Eds. (American Geophysical Union, Washington DC, 2000), pp. 63–87.
38. M. Ishii, J. Tromp, *Phys. Earth Planet. Inter.* **146**, 113 (2004).

39. The Advanced Light Source is supported by the Director, Office of Science, Office of Basic Energy Sciences, and Materials Sciences Division of the U.S. Department of Energy under contract DE-AC02-05CH11231. This research was partially supported by the Consortium for Materials Properties Research in Earth Sciences under NSF Cooperative Agreement EAR 06-49658. L.M. acknowledges support of the Bateman Fellowship at Yale University. H.R.W. acknowledges support from CDAC and NSF grants EAR0836402 and EAR0757608. We thank S. Gaudio, C. Lesher, S. Clark, J. Knight, and J. Yan for technical assistance. Comments from three anonymous reviewers improved the manuscript.

Supporting Online Material

www.sciencemag.org/cgi/content/full/329/5999/1639/DC1
Materials and Methods
Figs. S1 and S2
Tables S1 and S2
References

18 May 2010; accepted 20 August 2010
10.1126/science.1192465

Genetic Restoration of the Florida Panther

Warren E. Johnson,[1]*† David P. Onorato,[2]*† Melody E. Roelke,[3]* E. Darrell Land,[2]* Mark Cunningham,[2] Robert C. Belden,[4] Roy McBride,[5] Deborah Jansen,[6] Mark Lotz,[2] David Shindle,[2] JoGayle Howard,[8] David E. Wildt,[8] Linda M. Penfold,[9] Jeffrey A. Hostetler,[10] Madan K. Oli,[10] Stephen J. O'Brien[1]†

The rediscovery of remnant Florida panthers (*Puma concolor coryi*) in southern Florida swamplands prompted a program to protect and stabilize the population. In 1995, conservation managers translocated eight female pumas (*P. c. stanleyana*) from Texas to increase depleted genetic diversity, improve population numbers, and reverse indications of inbreeding depression. We have assessed the demographic, population-genetic, and biomedical consequences of this restoration experiment and show that panther numbers increased threefold, genetic heterozygosity doubled, survival and fitness measures improved, and inbreeding correlates declined significantly. Although these results are encouraging, continued habitat loss, persistent inbreeding, infectious agents, and possible habitat saturation pose new dilemmas. This intensive management program illustrates the challenges of maintaining populations of large predators worldwide.

Pumas (also called cougars, mountain lions, or panthers) are currently distributed throughout western North America and much of Central and South America (*1*). The endangered Florida panther (listed in 1967, table S1), the last surviving puma subspecies in eastern North Amer-